chemosensors

Article

Eu-Doped Nickelate as a Platform for an Enzyme-Based Resistive Biosensor for Glucose

Gilson P. Lopes [1], Jéssica H. H. Rossato [1], Neftali L. V. Carreno [2,3], Iseli L. Nantes [4] and Marcia T. Escote [1,*]

[1] Centro de Engenharia, Modelagem e Ciências Sociais Aplicadas, Universidade Federal do ABC, Santo André CEP 09210-580, SP, Brazil; gilson.lopes@ufabc.edu.br (G.P.L.); jhelisahr@gmail.com (J.H.H.R.)
[2] Graduate Program in Materials Science and Engineering, Technology Development Center, Federal University of Pelotas, Pelotas CEP 96010-610, RS, Brazil; neftali@ufpel.edu.br
[3] Center for Embedded Devices and Research in Digital Agriculture (CEDRA), SENAI, 3239 Getúlio Vargas Avenue, São Leopoldo CEP 93025-753, RS, Brazil
[4] Centro Ciências Naturais e Humanas, Universidade Federal do ABC, Santo André CEP 09210-580, SP, Brazil; ilnantes@ufabc.edu.br
* Correspondence: marcia.escote@ufabc.edu.br; Tel.: +55-11-4996-8232

Abstract

Nickelate oxides show promise for biosensing applications, especially in glucose detection. Creating nickelate-based biosensors involves utilizing their electron-correlated structure and the metal–insulator (MI) transition, which endows them with unique electronic, magnetic, and catalytic properties. Chemical or oxygen vacancies can alter their conductivity and catalytic activity, enabling redox-based detection. In this study, $Nd_{1-x}Eu_xNiO_3$ films ($0 < x < 0.35$) functionalized with Glucose Oxidase (GOx) were tested for glucose sensing. Eu substitution shifts the MI transition temperature (T_{MI}) from 200 K (x = 0) to 340 K (x = 35). At room temperature, these films undergo a metallic-to-insulator phase transition, which, along with the Ni^{3+}/Ni^{2+} ratios, influences their sensing capabilities. Time-resolved electrical resistance measurements monitored how glucose interacts with the film surfaces. The sample with x = 0.3 exhibited a measurable resistance change in response to glucose concentrations ranging from 10^{-12} to 0.5 M, with a sensitivity of 9.1 mM^{-1} and a limit of detection (LOD) of approximately 0.47 µM. Reproducibility and interference tests with other sugars yielded good results across all samples. Eu doping in $NdNiO_3$ enhances their sensing response, highlighting the importance of electronic state and MI transition in the sensing performance of these nickelate-based glucose sensors.

Keywords: glucose biosensors; rare-earth nickelates; $NdNiO_3$; enzymatic biosensors; electrochemical biosensors; metal-insulator transition

check for updates

Received: 1 July 2025
Revised: 21 October 2025
Accepted: 23 October 2025
Published: 3 November 2025

Citation: Lopes, G.P.; Rossato, J.H.H.; Carreno, N.L.V.; Nantes, I.L.; Escote, M.T. Eu-Doped Nickelate as a Platform for an Enzyme-Based Resistive Biosensor for Glucose. *Chemosensors* **2025**, *13*, 387. https://doi.org/10.3390/chemosensors13110387

Copyright: © 2025 by the authors. Licensee MDPI, Basel, Switzerland. This article is an open access article distributed under the terms and conditions of the Creative Commons Attribution (CC BY) license (https://creativecommons.org/licenses/by/4.0/).

1. Introduction

Glucose is an essential carbohydrate in the human body, involved in crucial metabolic processes such as oxidative phosphorylation and glycolysis, which contribute to the synthesis of proteins, glycogen, and lipids [1,2]. However, one of the main diseases associated with this carbohydrate is diabetes, a common disease that requires monitoring the glucose level accurately, sensitively, reliably, quickly, and in a way that allows the patient to measure it daily [3]. Typically, in glucose monitoring, glucose/enzyme reactions produce hydrogen peroxide (H_2O_2), which, despite being an unstable molecule, can be harmful, for example, during the metabolism of proteins and carbohydrates, among other processes.

Various analytical methods have been proposed to measure glucose levels in different body fluids, classified by their invasiveness (invasive, minimally invasive, or non-invasive

techniques). In both blood and sweat analysis, various methods, including spectroscopy, electrochemistry, and chromatography, are effectively used in different studies, providing high-sensitivity and selectivity results [4–7].

These glucose sensors are classified by their working principles into two types: non-enzymatic and enzymatic. Both promote glucose oxidation, leading to changes in the sensor's electrical signal response [4]. In enzymatic sensors, glucose is detected indirectly by the formation of H_2O_2. Conversely, non-enzymatic sensors utilize nanomaterials, such as metals and metal oxides, to mimic enzymatic properties and modify the properties of the analyte [4,8]. The glucose oxidase (GOx) enzyme is commonly used in glucose sensors because of its high specificity and selectivity. Typically, enzymatic sensing involves the transfer of electrons during oxidation reactions between GOx and glucose. Specifically, GOx, which contains flavin adenine dinucleotide (FAD), catalyzes the conversion of glucose to gluconolactone and reduces GOx-FAD to GOx-FADH2. This reaction produces current or voltage changes that are usually measured at the electrode [4]. The main challenges in developing enzymatic glucose sensors include immobilizing GOx on the electrode and preventing its denaturation and deactivation due to changes in pH or temperature [7].

In glucose non-enzymatic sensors, metal oxides like CuO_2 nanoparticles serve as electrocatalysts to transfer electrons during glucose oxidation. It is not a straightforward reaction that happens in several steps, depending on the materials. Generally, CuO_2 is converted into CuOOH, which reacts with glucose to produce $Cu(OH)_2$ and gluconic acid [4]. The advantage of these sensors is their stability; however, their drawbacks include low selectivity and reproducibility, mainly due to low conductivity or high agglomeration [7].

There are different types of enzymatic and non-enzymatic glucose sensors, which have been combined with various nanomaterials. Recently, GOx combined with nanomaterials and Au-MoS_2 peroxidase (POD)-like nanoenzymes has been used in glucose sensors [8–10]. Non-enzymatic glucose sensors have been extensively studied using metal and metal oxide nanostructures to enable their application in glucose detection sensors. Among these materials, we can include nanocubes and nanospheres of Fe_3O_4 coated with SiO_2 and functionalized with poly(acrylic) acid to detect proteins [11], metal oxide nanoparticles such as CuO, Cu_2O, MnO_2, NiO, CoO_x [4,12–14], carbon-based and composite materials [7,15,16] and perovskite oxides like $Sr_{0.85}Ce_{0.15}FeO_3$, $La_{1-x}Sr_xMnO_3$ ($0.1 < x < 0.6$), $RNiO_3$ (R = La, Nd, Sm) [9,17–20]. The advantages of using perovskite oxides include the ability to control their physical properties through doping, their low electrical conductivity, and the presence of oxygen vacancies in their crystal structure. These features contribute to their capacity to catalyze the oxidation process or to serve as glucose sensors.

Perovskite nickelates $RNiO_3$ (R = rare earth) display significant physical properties that are directly linked to their crystalline and electronic structures [21]. Usually, these compounds ($R \neq La$) undergo a metal–insulator transition (MIT), which is highly sensitive to changes in composition, doping, and lattice strain. These features enable the customization and enhancement of the electronic and chemical properties of the nickelate for specific sensing applications [9,10,22–24].

At low temperatures, $RNiO_3$ ($R \neq La$) compounds exhibit an insulator state, and a metal–insulator transition (MIT) occurs during heating, leading to metallic behavior above the MIT temperature (T_{MI}). At T_{MI}, their perovskite orthorhombic distorted structure (*Pbnm*) typically shifts to a monoclinic symmetry ($P21/n$), with two different Ni-O bond lengths, and the paramagnetic state transitions into an antiferromagnetic order [25]. When this electronic localization happens, a charge disproportionation $2Ni^{3+} \rightarrow Ni^{3+\delta} + Ni^{3-\delta}$ is observed, establishing a charge-ordered (CO) state. The Ni-O-Ni bond angle plays a key role in predicting the electronic bandwidth and magnetic interactions. A smaller rare earth cation causes a more distorted structure, which is observed to result in a monotonic

increase in the MIT temperature as the ionic radius of the rare earth cations decreases; these values range from 145 K (Pr) to 500 K (Lu), respectively [26]. For R = Pr and Nd, the T_{MI} is close to the magnetic ordering temperature (T_N); for other rare earth cations, such as R = Sm, Eu, T_{MI} exceeds T_N. Consequently, as the size of the rare earth cation decreases in $RNiO_3$, the Ni-O-Ni bond angle and the overlap of O 2p and Ni 3d bands decrease, which also causes rotation of NiO_6 octahedra and influences MIT and related properties of these compounds.

It is noteworthy that the thermally driven T_{MI} exhibited by the nickelates has a rich phase diagram, while the magnetic and electronic properties can be controlled by the size of the rare earth cation. It should also be noted that these $RNiO_3$ compounds are challenging to obtain in bulk because they must retain the unstable Ni^{3+} state, which requires high oxygen pressure during synthesis. Generally, producing $RNiO_3$ thin films involves low or partial oxygen pressures, but this can also lead to the formation of non-stoichiometric oxygen in these materials films [27].

It is important to note that synthesizing $RNiO_3$ compounds in bulk form is very challenging because maintaining the unstable Ni^{3+} oxidation state requires high oxygen pressure during synthesis. Typically, $RNiO_3$ thin films are prepared under lower or partial oxygen pressures. However, this often causes the films to have non-stoichiometric oxygen, which affects their final composition and properties. Oxygen vacancies in $RNiO_3$ compounds can affect their magnetic, structural, and electronic properties. Their presence causes elongation of the Ni-O bonds and bending of the Ni-O-Ni angles, impacting their charge ordering [21].

Due to their exceptional properties, nickelates are used as sensing materials for various biochemical compounds, including glucose, glutamate, ascorbic acid, and trifluoperazine [9,10,27,28]. $LaNiO_3$ nanofibers and $NdNiO_3$ nanoparticles were used as electrodes in a non-enzymatic glucose sensor that exhibits high selectivity and sensitivity [17,19]. Here, the electro-oxidation mechanism of the catalytic oxidation of glucose involves the transformation of Ni^{2+} to Ni^{3+}, which oxidizes glucose into gluconolactone and reduces the metal back to Ni^{2+}. A similar result can be observed in non-enzymatic ascorbic acid biosensors made from $NdNiO_3$ nanotubes synthesized at ambient oxygen pressure, which contain Ni^{3+}/Ni^{2+} and oxygen vacancies [28]. This electronic configuration facilitates charge transfer between the oxide nanotubes and ascorbic acid, resulting in the oxidation of ascorbic acid to form dehydroascorbic acid. Doped nickelate, such as $LaNi_{0.6}Co_{0.4}O_3$ nanoparticles, was also used as electrodes for sensing devices to detect glucose and H_2O_2 in blood serum [29].

As observed in thin film platforms of $SmNiO_3$ and $NdNiO_3$/Nafion, which were used for studying enzymatic glucose and glutamate biosensors for constructing neurotransmitters, the glucose oxidase enzyme is attached to the Au-$SmNiO_3$ substrate [9,10]. The oxidation mechanism involves the transfer of hydrogen atoms from glucose to the GOx enzyme and then into the electronic structure of the nickelate. Zhang et al. [9] describe that these hydrogen bonds with oxygen anions and occupy interstitial sites of the NiO_6 octahedra in $SmNiO_3$, changing the occupancy of the Ni e_g orbitals and affecting its electrical resistance. The GOx role is to mediate the glucose oxidation reaction without external energy input.

In this context, we synthesized $Nd_{1-x}Eu_xNiO_3$ thin films (x = 0, 0.30, and 0.35) using the chemical solution deposition method at low temperature and ambient oxygen pressure. It should be noted that the synthesis of these nickelate films typically requires high oxygen pressure, so our initial challenge was to synthesize these films effectively. These films will also exhibit a mixture of oxidation states, Ni^{3+}/Ni^{2+}, and oxygen vacancies as observed by Rossato et al. [28], which can provide valuable insights. Additionally, producing Eu-doped

$NdNiO_3$ thin films should shift the MI transition to temperatures between 200 K and 400 K. Most sensor studies were performed at room temperature in either the metallic state of $LaNiO_3$ or $NdNiO_3$, or in the insulating state of $SmNiO_3$. In this work, we analyze compounds with different electronic states of the metal, specifically the metal–insulator edge and the insulator state between the metallic and insulating phases. This demonstrates how the electronic state interacts with glucose/glucose oxidase and their potential as a platform for enzymatic glucose sensors.

2. Materials and Methods

2.1. Chemicals

Citric Acid, ethylene glycol, $Ni(CH_3CO_2)_3.4H_2O$, $Nd(CH_3CO_2)_3.H_2O$, $Eu(CH_3CO_2)_3.H_2O$, Cysteamine, GOx enzyme (*Aspergillus niger*, type VII), H_2O_2 35% PA, and D-(+)-glucose. All reagents were of analytical grade and high purity, purchased from Sigma-Aldrich. Solutions were prepared using high-purity water (Direct-Q UV Ultra purification System, Millipore Sigma-Merck, Darmstadt, Germany). The phosphate buffer (PB) at pH 6.8 was used as the electrolyte.

2.2. Precursor Solution

The $Nd_{1-x}E_xNiO_3$ (x = 0.0; 0.30; 0.35) precursor solutions were prepared by dissolving stoichiometric amounts of Nd/Eu-Ni in aqueous citric acid at 70 °C with constant stirring. Then, hydrated neodymium acetate and hydrated europium(III) acetate were stirred into the solution until they were fully dissolved (~1 h). Ethylene glycol was added and maintained under these conditions for about 1 h to allow for the complexation of metal ions and subsequent polyesterification. Previously, the viscosity of these solutions was adjusted to approximately 5 cP using a digital viscometer (Brookfield Viscometer DV-I Prime).

$Nd_{1-x}Eu_xNiO_3$ Film Deposition

Before the deposition process, the $Si(100)/SiO_2$ substrates were cleaned with strong acids and bases, along with H_2O_2 to remove possible contamination from organic residues. The precursor solutions were applied to the substrates using a spin coater (KW-4A, Chemat Technology—SPI supplies, West Chester, PA, USA), spinning at 3000 rpm for 3 s and then at 7000 rpm for 20 s. The films were dried at approximately 50 °C for 10 min to eliminate solvents. To achieve film thicknesses ranging from 200 to 400 nm, six layers of each composition were deposited for all samples. Each layer was heat-treated at 300 °C for 2 h and then at 700 °C for 4 h in a tubular electric furnace (Lindberg Blue M, Thermo Fisher Scientific, Waltham, MA, USA) within an oxygen atmosphere (O_2). The samples are designated as $NdNiO_3$ (NNO), $Nd_{0.7}Eu_{0.3}NiO_3$ (NENO30), and $Nd_{0.65}Eu_{0.35}NiO_3$ (NENO35).

2.3. Apparatus and Procedures

All films were characterized by X-ray powder diffraction (XRD) using a D8-Focus diffractometer (Bruker AXS, GmbH, Billerica, MA, USA) equipped with a LynxEye 1D linear silicon strip detector and Cu-Kα radiation (λ = 1.54056 Å). All measurements were conducted at room temperature (25 °C), with scans from 20° to 60°. Fourier-transform infrared spectroscopy of these samples was performed using a Model 610-IR spectrophotometer (Varian—Agilent Techn., Palo Alto, CA, USA) with the PIKE diffuse reflectance accessory, covering the wavenumber range of 500 to 4000 cm^{-1} and a resolution of 4.0 cm^{-1}. A field emission scanning electron microscope (JMS-6701F, JEOL, Tokyo, Japan), was used to analyze the homogeneity and structure of each $Nd_{1-x}Eu_xNiO_3$ thin film. X-ray photoelectron spectroscopy (XPS) was conducted with a Thermo Scientific K-Alpha+ spectrometer using Al Kα radiation. Spectral analysis was performed using CasaXPS software (2020, version 2.3.23PR1.0). The C 1 s peak (284.6 $\pm$ 0.1 eV) served as the reference for energy

calibration. The background was corrected with a Shirley algorithm combined with a Lorentzian–Gaussian function. Absorption spectra were measured with a Cary 50 UV–Vis spectrophotometer (Varian—Agilent Techn., Palo Alto, CA, USA), covering the range of 200–1000 nm.

The electrical transport properties were measured by attaching copper terminals to the film's surface with silver epoxy paint, which was cured at 100 °C for 10 min. The films were then connected to the sample holder of the Quantum Design PPMS (Physical Properties Measurement System, Quantum Design, San Diego, CA, USA). R(T) measurements were also performed on an 204 ARS closed-cycle cryostat (Advanced research system, Macungie, PA, USA) linked to a measurement system (Keithley SourceMeter 2400 (Tektronix, Cleveland, OH, USA), 331 temperature controller (Lake Shore Cryotronics, Woburn, MA, USA) and a microcomputer via GPIB/USB connection, using LabVIEW (version 10.0.1, 2010).

2.4. Bio-Interface

The first stage of this assembly involved depositing gold tracks on the surface of the $Nd_{1-x}Eu_xNiO_3$ films, using a lab-made thermal evaporation system to achieve a thickness of about 100 nm. To functionalize the films with GOx, we followed a protocol described in the literature that uses cysteamine to attach an oxidized GOx enzyme [9,10]. First, the samples were immersed in a 10 mM cysteamine (CysAm) solution for 2 h in a dark room at room temperature. They were then rinsed with water to remove unreacted cysteamine and dried in a spin coater.

Before depositing in the NNO/Au/CysAm or NENO/Au/CysAm, an oxidation step was performed on the GOx enzyme to stabilize it. For this, a pH 6.8 buffer of 0.1 M sodium phosphate was prepared for enzyme oxidation [9]. A 20 µM GOx solution was prepared by adding 30 mg of sodium metaperiodate to 5 mL of buffer. The solution was incubated for 1 h at 4 °C, then 6.97 µL of ethylene glycol was added to stop the reaction, followed by another 30-min incubation at room temperature. The product was purified through membrane dialysis for 24 h to collect oxidized GOx and exchange the buffer to 0.1 M PB at pH ~6.8. Finally, the NNO/Au/CysAm and NENO/Au/CysAm devices were immersed in this GOx solution for about 1 h at 4 °C, then rinsed with deionized water. The devices were dried in a spin coater and stored at 4 °C in the refrigerator (see Supplementary Materials).

To observe the effects of these modifications with CysAm/GOx, the sample surfaces were examined using Atomic Force Microscopy (NanoIR—NovaVista, Molecular Vista, San Jose, CA, USA) before and after functionalization. The charge transfer on glucose and nickelate film surfaces was analyzed by monitoring resistance responses over time, as expected with glucose solutions of different concentrations. These measurements were also conducted using a Keithley 2400C Sourcemeter (Tektronix, Cleveland, OH, USA) connected to a PC via the LabVIEW (version 10.0.1, 2010) interface. All these measurements were repeated at least three times on four samples of NNO, NENO30, and NENO35 films.

Direct analysis of glucose in orange juice samples was performed to verify the applicability of the proposed method in real sample analysis. For this, we prepared samples of commercial and freshly squeezed orange juice (OJ). All samples were filtered using a 45-micron syringe filter. The commercial OJ reported a sugar concentration of 9 g/100 mL, whereas the glucose content is approximately 2 g/100 mL. This OJ was diluted in water to reach concentrations ranging from 0.05 to 0.4 M and used to build the calibration curve.

3. Results

3.1. Structural, Morphological, and Electrical Characterization of $Nd_{1-x}Eu_xNiO_3$ Films

Figure 1i displays the XRD patterns of NNO, NENO30, and NENO35 films, indicating they are polycrystalline samples. The Bragg reflections are identified as belonging to

the $NdNiO_3$ crystalline phase (space group symmetry *Pbnm*; JCPDF 01-080-1947) [30]. Moreover, as expected, replacing Nd^{3+} with Eu^{3+} does not alter the symmetry of the crystalline structure. The lattice parameters, estimated and listed in Table 1, differ from those of bulk samples; these cell parameters are slightly larger than the bulk cell parameter a = 5.3891 Å but smaller than b = 5.3816 Å and c = 7.6101 Å reported in the literature. This variation is more noticeable when comparing the unit cell volume (V). Additionally, the samples were heat-treated at low temperatures under an oxygen pressure of about 1 bar. Oxygen non-stoichiometry likely increases due to Eu^{3+} replacing Ni^{3+} in the lattice, leading to a mixture of Ni^{3+} and Ni^{2+}. Figure 1iii shows a schematic band structure and the orthorhombic structure for all samples; these crystal structures were modeled using Vesta software (2024, version 2.1.6) based on literature data.

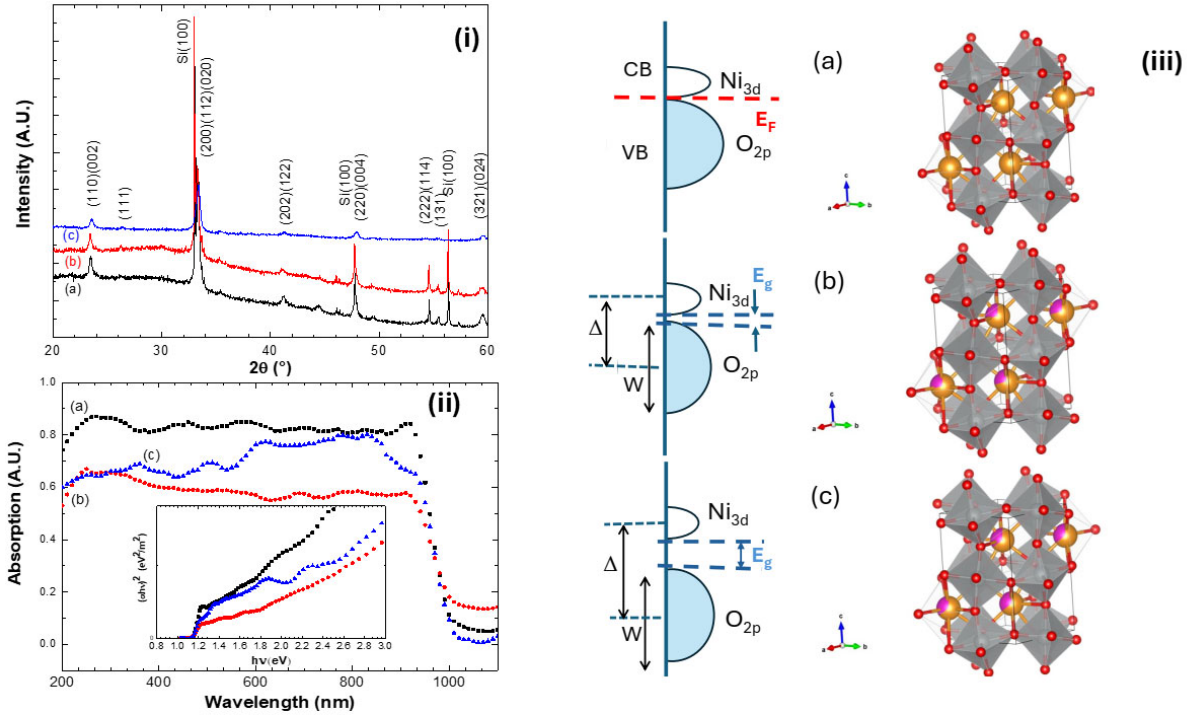


Figure 1. (**i**) X-ray diffractograms, (**ii**) UV–vis spectroscopy, and the inset shows the Tauc plot. (**iii**) Schematic charge-transfer band structure and orthorhombic structure of (**a**) NNO films, (**b**) NENO30, and (**c**) NENO35 deposited on SiO_2/Si(100) substrate. Here, E_F is Fermi energy, Δ is the charge transfer energy, W is the O 2p bandwidth, the red circles represent the oxygen atoms, the yellow circles the Nd atoms, and the purple circles the Eu atoms.

Table 1. The values listed were the pseudo-cubic lattice parameters (a_{pc}), unit cell volume (V), the crystallite size (D), and tension at the film/substrate interface (e), for the $Nd_{1-x}Eu_xNiO_3$ films.

x	a_{pc} (Å)	V (Å^3)	D (nm)	ε (%)
0.0	3.800(31)	232(2)	135(1)	−0.300
0.3	3.801(35)	232(2)	135(1)	−0.300
0.35	3.792(38)	231(2)	95(1)	−0.301
$NdNiO_3$-Bulk [30]	3.81	220.71		

The film/substrate interfacial strain (e) and crystallite sizes of the synthesized materials were also reported, following the reduction behavior for the most substituted compounds. The film thickness may also have influenced these values, considering the growth method, which generally produces films with a thickness of around 200–400 nm, exceeding the film thicknesses reported in the literature.

UV–vis spectroscopy measurements show how replacing Nd^{3+} with Eu^{3+} affects the electronic structure of these films (Figure 1ii). As mentioned, decreasing the radius of the element replacing Nd in perovskite compounds can significantly affect the electronic structure of nickelate materials, since this substitution can cause rotations, twists, and distortions of the NiO_6 octahedra that comprise the crystal lattice. The absorption range from 700 to 1200 nm corresponds to excitation from the occupied to the unoccupied state of the transition metal Ni e_g* antibonding orbital. Below 700 nm, absorption results from transitions from the hybridized t_{2g}*/2p oxygen orbitals to the e_g* orbitals [31,32].

The inset of Figure 1ii shows the curves of the Tauc method, revealing that three distinct slopes are noticeable for these films, indicating changes in their electronic structures [31]. The slopes above 3 eV changes are related to the transition from metallic to insulating electronic states, promoted by Eu substitution in the $NdNiO_3$ compound. It is important to note that the measurements were taken at room temperature (~25 °C). According to the literature, at room temperature, the NENO35 film is in the insulating phase, while the others are either in the metallic phase or at the metal–insulator transition region [33].

Figure 2 shows the FESEM images of the surfaces of $Nd_{1-x}Eu_xNiO_3$ films ($0 \leq x \leq 0.35$). These images reveal homogeneous surfaces, low packing density, and few defects, with particles that are roughly rounded and slightly elongated, ranging from 50 to 120 nm in length. Similar results were observed in the work of Nikulin and Tiwari, where the synthesis of small, weakly linked crystallites was studied. The estimated average particle diameters are 56.0(6) nm, 77.4(8) nm, and 82.5(8) nm for NNO, NENO30, and NENO35, respectively (see Figure S1). These analyses indicate that the average particle diameter increases with higher Eu substitution in the $NdNiO_3$ matrix, which is expected since the substituent species has a relatively larger ionic radius.

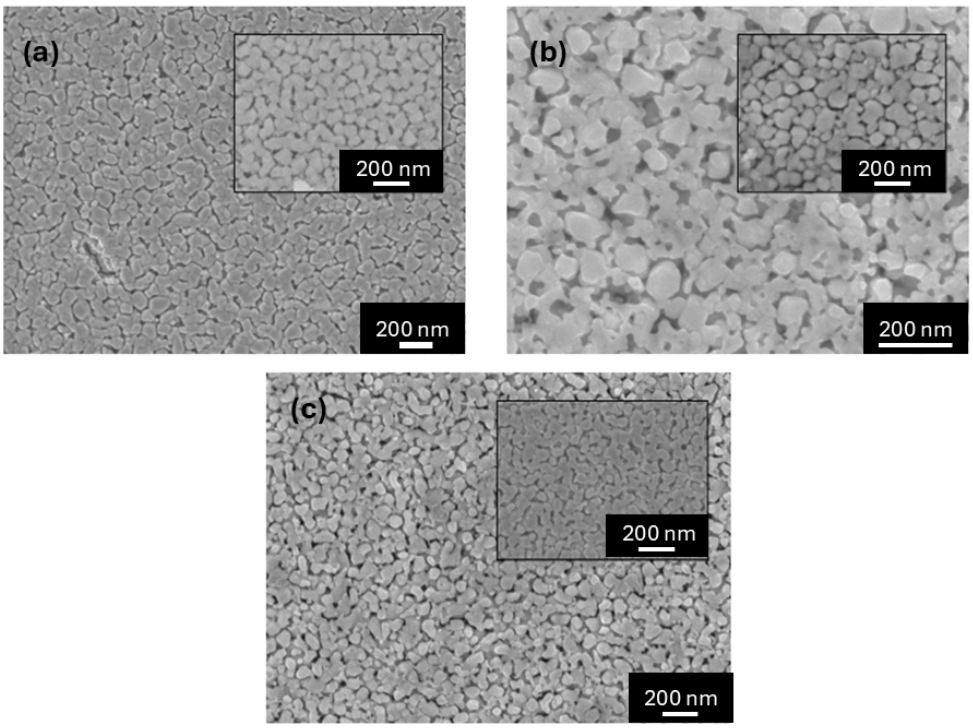


Figure 2. FESEM images of sample surfaces of (**a**) NNO, (**b**) NENO30, and (**c**) NENO35 films deposited on SiO_2/Si(100) substrate with 6 layers of deposition. Inserts show images with higher magnification.

To assess the impact of Ni^{2+}/Ni^{3+} states and oxygen vacancies on the physical properties of Eu-doped $NdNiO_3$ thin films, XPS measurements were performed. Figure 3a shows the XPS survey spectra of NNO, NENO30, and NENO35 samples. The survey spectra dis-

play characteristic peaks for Nd, Ni, and O elements. In the NENO30 and NENO35 spectra, additional signals corresponding to Eu (highlighted in gray) are observed, confirming the successful doping of Eu into the films, which agrees with the XRD and transport data.

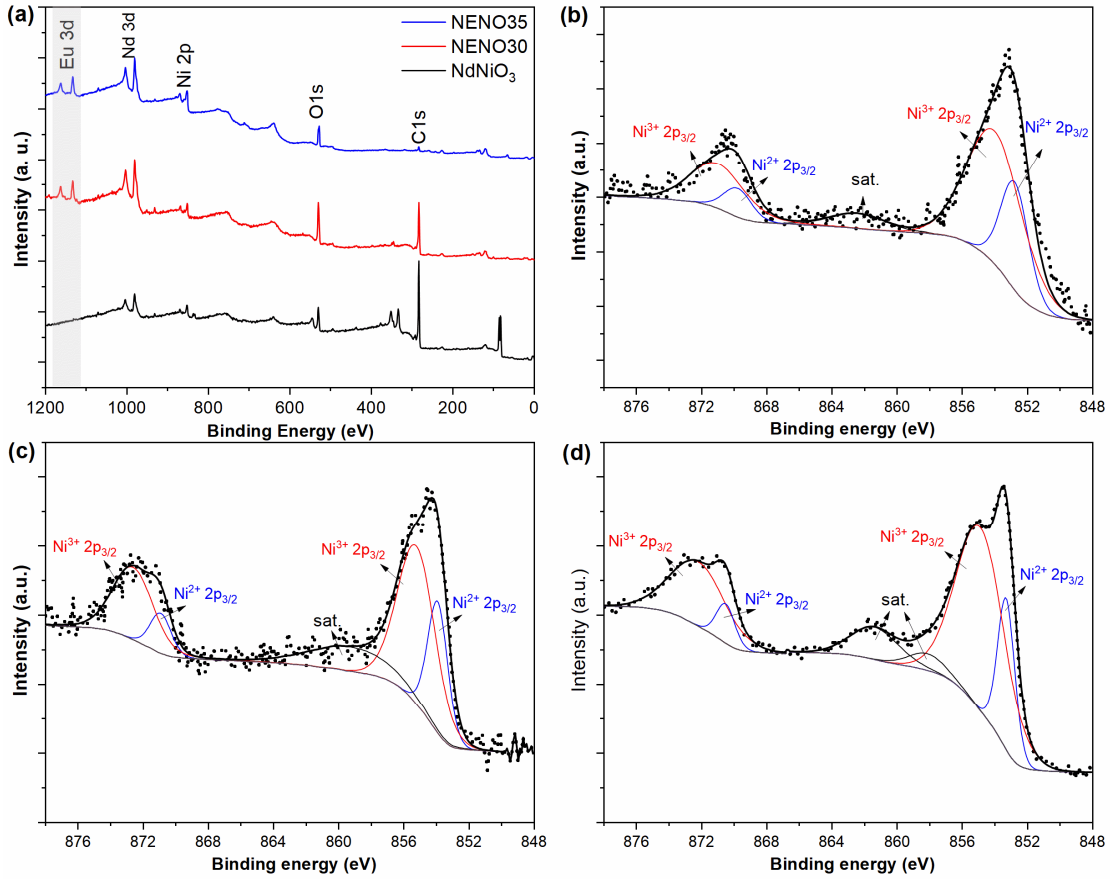


Figure 3. XPS survey spectra (**a**) and high-resolution XPS spectrum of Ni 2p (**b**–**d**) from NNO, NENO30, and NENO35 films, respectively.

As reported in previous XPS analyses of NNO nanostructures, the presence of Ni^{2+} can cause significant changes in the properties and characteristics of these compounds [34–36]. Figure 3b shows the Ni 2p high-resolution core-level spectrum of NNO. The spectrum exhibits four peaks: the peaks at 852.8 and 854.0 eV are attributed to Ni^{2+} $2p_{3/2}$ and Ni^{3+} $2p_{3/2}$, respectively, while the peaks at 867.8 and 871.0 eV correspond to Ni^{2+} $2p_{1/2}$ and Ni^{3+} $2p_{1/2}$, respectively. The Ni 2p high-resolution spectra of NENO30 and NENO35 are shown in Figure 3c,d. For the NENO30 sample, the $2p_{3/2}$ and $2p_{1/2}$ doublet related to Ni^{2+} and Ni^{3+} were fitted at 853.9 (870.9) eV and 855.2 (872.6) eV, respectively. In the case of NENO35, the corresponding Ni^{2+} and Ni^{3+} peaks were fitted at 853.3 (870.5) eV and 854.9 (872.2) eV, respectively. Based on the peak deconvolution of the Ni 2p spectra, the Ni^{2+}/Ni^{3+} ratio was estimated by comparing the relative areas of the Ni^{2+} $2p_{3/2}$ and Ni^{3+} $2p_{3/2}$ peaks. The NNO, NENO30, and NENO35 exhibited Ni^{2+}/Ni^{3+} ratios of 0.40, 0.44, and 0.30, respectively. These results reveal that a mixture of bi- and trivalent Ni was stabilized during thermal treatment of the thin films with an O_2 pressure of approximately 1 atm, which is insufficient for the primary stabilization of Ni^{3+} in the $RNiO_3$ phase [33].

Figure 4 shows the normalized electrical resistance curves as a function of temperature for $Nd_{1-x}Eu_xNiO_3/SiO_2/Si(100)$ films during cooling and heating. The R(T)/R(300 K) versus temperature curves exhibit metallic behavior above the Metal–Insulator Transition (T_{MI}) temperature, indicated by a decrease in resistance during cooling. Below T_{MI}, the material enters an insulating state, with R(T) values increasing by several orders of magnitude as

the temperature drops [37,38]. Hysteresis is also observed between the heating and cooling curves for the three analyzed films. An important point is that the T_{MI} temperature was controlled by increasing the replacement of Nd^{3+} by Eu^{3+}, as expected from bulk studies reported in the literature [33,39].

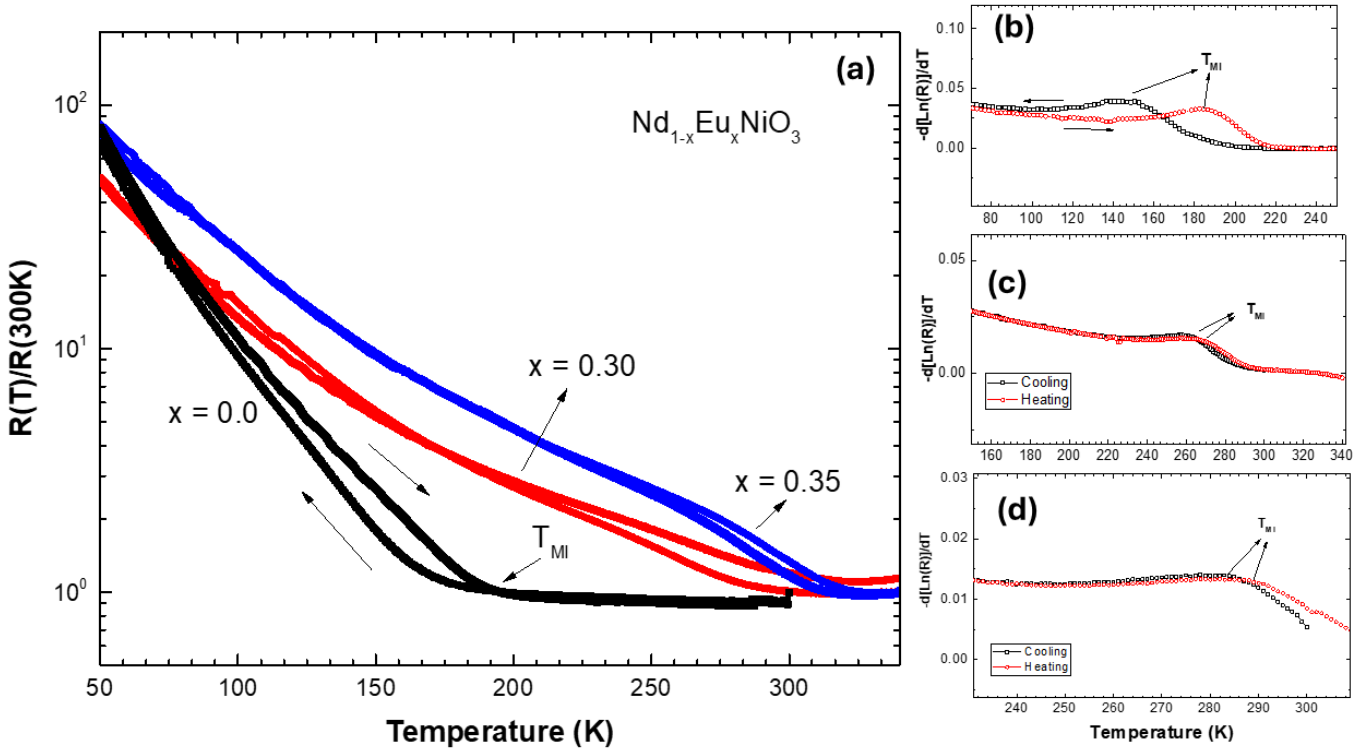


Figure 4. Temperature dependence R(T)/R(300K) curves measured for $Nd_{1-x}Eu_xNiO_3/SiO_2/Si(100)$ films (**a**). Curves of -d(Ln(R))/dT versus temperature for samples (**b**) NNO, (**c**) NENO30, and (**d**) NENO35.

Generally, using electrical resistivity measurement curves versus temperature allows the study of properties such as the Metal–Insulator Transition (T_{MI}) and the material's behavior. The power law can describe the temperature dependence of the electrical resistance: $\rho(T) = A + BT^n$, where A is the residual electrical resistivity constant, B is the temperature-related coefficient, and n is the power factor, which generally takes on values of 1 or 2. In the NNO sample, n is 3/2 for temperature ranges between 200 and 340 K, and the scattering can be linked to electron–phonon coupling. Below the T_{MI}, the behavior becomes more complex, as there is a coexistence region of metallic and insulating phases (hysteresis region), and the Arrhenius law cannot describe the region with the highest proportion of insulating phase [$\rho(T) = \rho_0 \exp(E_g k_B/T)$.].

The T_{MI} values obtained for each sample during heating and cooling were estimated by calculating $-$d[lnR(T)]/dT, with the T_{MI} peak indicated in Figure 4b–d. The values are comparable to those reported in the literature [39]. The films exhibit T_{MI} ranging from 190 K to 280 K from x = 0 to x = 0.35. As shown, increasing the Eu concentration in the prepared films results in a higher phase transition temperature, as expected [33]. These results are like those reported in the literature and agree with the schematic band structure of Figure 1iii. Therefore, these samples provide nickelate platforms with three different electronic states: metallic, intermediate, and insulating at room temperature (300 K).

3.2. $Nd_{1-x}Eu_xNiO_3$ as a Platform for Biosensors

To demonstrate the potential of $Nd_{1-x}Eu_xNiO_3$ films for sensor applications, they were functionalized with GOx-modified Au electrodes and characterized. A schematic diagram

of this device is shown in Figure 5a. AFM images confirmed the effect of CysAm/GOx on the gold electrode deposited on the nickelate films. The surface morphology of both pristine and GOx-modified electrodes is shown in Figure 5b,c. The pristine electrode has an average grain diameter (D) of approximately 22 nm and a roughness (R) of about 5.2 nm. In comparison, the GOx-decorated electrode shows D around 10.5 nm and R around 3.1 nm. The smooth topography seen in Figure 5c and the reduction in grain size suggest that GOx molecules are associated with several bright spots covering the gold surface. However, the average size and height of GOx molecules, around 10 nm, are larger than the 4–5 nm reported in the literature [9]. Their size depends on how cysteamine modifies the surface and the prior topography of the gold electrode.

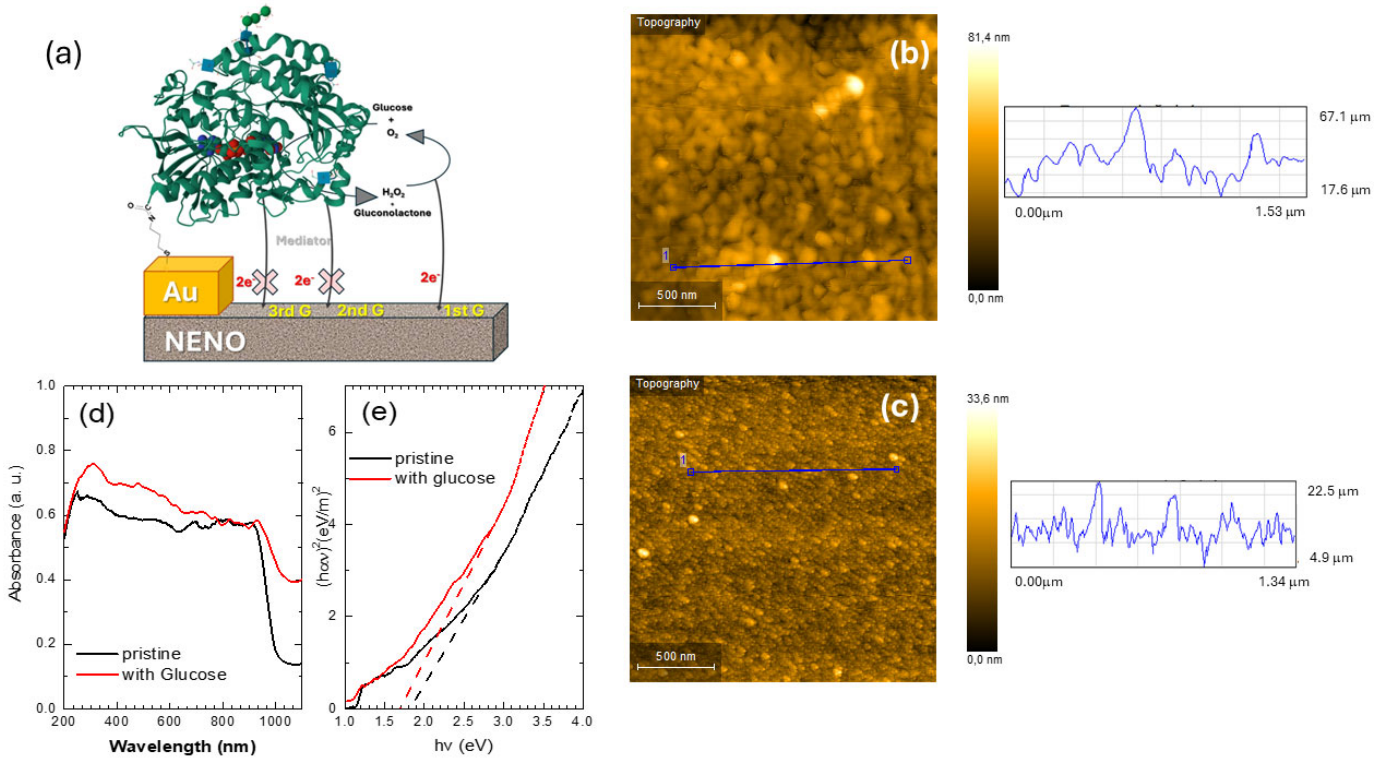


Figure 5. (**a**) Schematic representation of the enzymatic NENO sensor configuration. The GOx (3QVR structure available in the Protein Data Bank) chain is represented by a green cartoon, and the cofactor FAD is represented by a spacefill model colored by atom element. The protein structure is bound to the gold surface by the adduct cysteamine. Electron transfer ($2e^-$) from the enzymatic reaction to NENO is facilitated by hydrogen peroxide produced through the reoxidation of FADH2 by molecular oxygen, characterizing a first-generation sensor (1stG). The sensor components are represented out of scale for clarity. (**b**) AFM scans of the pristine and (**c**) GOx-modified gold electrode deposited on the NENO35 film. The blue lines represent the line scan showing the surface height variation on the NENO30 sample. (**d**) UV–vis spectra, and (**e**) estimated Tauc graph of samples for NENO30/Au/CysAm film decorated with GOx before (pristine) and after deposition of a 0.5 M glucose solution on the surface. The dashed red and black lines indicate changes in the absorption slopes.

Firstly, the interaction of the GOx/CysAm-modified nickelate film with glucose was investigated using Fourier Transform Infrared (FTIR) and UV–vis spectroscopy measurements before and after exposure to glucose. The FTIR spectrum is shown in Figure S2a. The gluconolactone band around 1135 cm^{-1} was not detectable when only a low concentration of this substance was used. The UV–vis spectra, before and after the reaction with the glucose solution, exhibit a slight shift towards longer wavelengths of the ~1000 nm absorption bands (see Figure 5d). The Tauc analysis was performed to verify this point. Figure 5e shows the Tauc plots derived from the UV-vis spectra GOx/NENO30 film; the glucose

reaction with the GOx/NENO30 film modifies the slope of the Tauc curve. Here, these curves reveal three slopes: one from 1 to 1.2 eV and another from 1.2 to 3 eV, both of which are assigned to excitations from occupied to unoccupied antibonding e_g* orbitals. These slopes don't seem to change significantly with the addition of glucose. The third slope, from 3 to 4.5 eV, is attributed to transitions from the O 2p orbitals to the Ni 3d e_g orbitals, and its slope slightly increases from 3.5 to 4.1 eV.m^{-2} [32]. Therefore, the intercept with the x-axis of both curves, without and with glucose, slightly decreases, which can be attributed to the nickelate–GOx reaction with glucose (see the black and red dashed lines in Figure 5e). Since, in this reaction, hydrogen doping of the nickelate–GOx device donates electrons to the e_g orbital. This can result in a significant on-site Coulomb repulsion between 3d e_g orbitals, promoting charge carrier localization, which can be related to these changes in the slope. Similar behavior was observed for the NNO and NENO35 samples. The temperature dependence of the electrical resistance R(T) of de NNO, NENO30, and NENO35 pristine, with CysAm, and GOx was measured. Similar behavior and T_{MI} were observed for all samples, with slight increases in the R(T) values (see for example Figure S2b).

Despite these findings, they do not confirm the mechanism related to the GOx-films oxidation of glucose based on this result. First, to verify the enzyme response, the GOx-NENO30 was soaked in a glucose solution, and the reaction product was analyzed in the presence of horseradish peroxidase (HRP) for different periods (see the Supplementary Materials, Figure S9). This result confirms the formation of H_2O_2 during the oxidation of glucose by GOx on the film's surface. In this reaction, the immobilized GOx catalyzes the oxidation of glucose, producing H_2O_2 and gluconic acid, which is a typical reaction of a first-generation glucose sensor (See Figure 5a) [4].

To evaluate the catalytic activity of these samples, 20 µL of 0.5 M glucose and 0.5 M hydrogen peroxide were applied separately to the surfaces of both the pristine and GOX-modified devices (see Figure 6i). The normalized electrical resistance R/R_0 (where $R_0 = R(t = 0s)$) was measured for 30 min at room temperature (~20 °C). The R/R_0 readings for nickelate films without enzyme remain almost constant (insert Figure 6i), indicating a slight increase in the R/R_0 values for all samples. This small change in R/R_0 values suggests that glucose was directly oxidized on the surface of the pristine film via the Ni^{2+}/Ni^{3+} redox transition (black curve), which enhances electron transfer and increases resistance. Additionally, dropping hydrogen peroxide and then glucose produces a similar increase in the R/R_0 values for all bare samples (red curve). Here, the nickelate film also promotes H_2O_2 oxidation to water through electron transfer. However, these small changes in R/R_0 could be related to a limited amount of H_2O_2 to transfer electrons on the surface of the nickelate film.

In contrast, the R/R_0 versus time curve for the GOx-coated samples shows a sharp increase after glucose addition (blue curve), suggesting a reaction between glucose and the nickelate/GOx device. Here, the enzymatic reaction between GOx and glucose continuously generates H_2O_2, which is consumed by electron transfer to the nickelate film and is quickly replenished until the system reaches a constant reaction rate. In contrast, the addition of hydrogen peroxide to the nickelate–GOx device results in a minor enhancement of the R/R_0 values, still, with a smaller magnitude than the result observed for the measurement with glucose (see Figure S5vi). The reaction mechanism behind the electrical response of the NENO/GOx films involves an initial transfer of an electron from the hydrogen peroxide produced by FADH2 reoxidation generated during the glucose-GOx reaction into the nickelate surface. As previously discussed, this reaction donates an electron to the Ni 3d orbital in the nickelate film, as indicated by the Tauc curves, suggesting charge carrier localization. These changes increase resistivity values, like those reported for $RNiO_3$

nanostructures [9,10]. Additionally, the presence of Ni^{3+}/Ni^{2+} and oxygen vacancies, as observed via XPS, contributes to this sensor response.

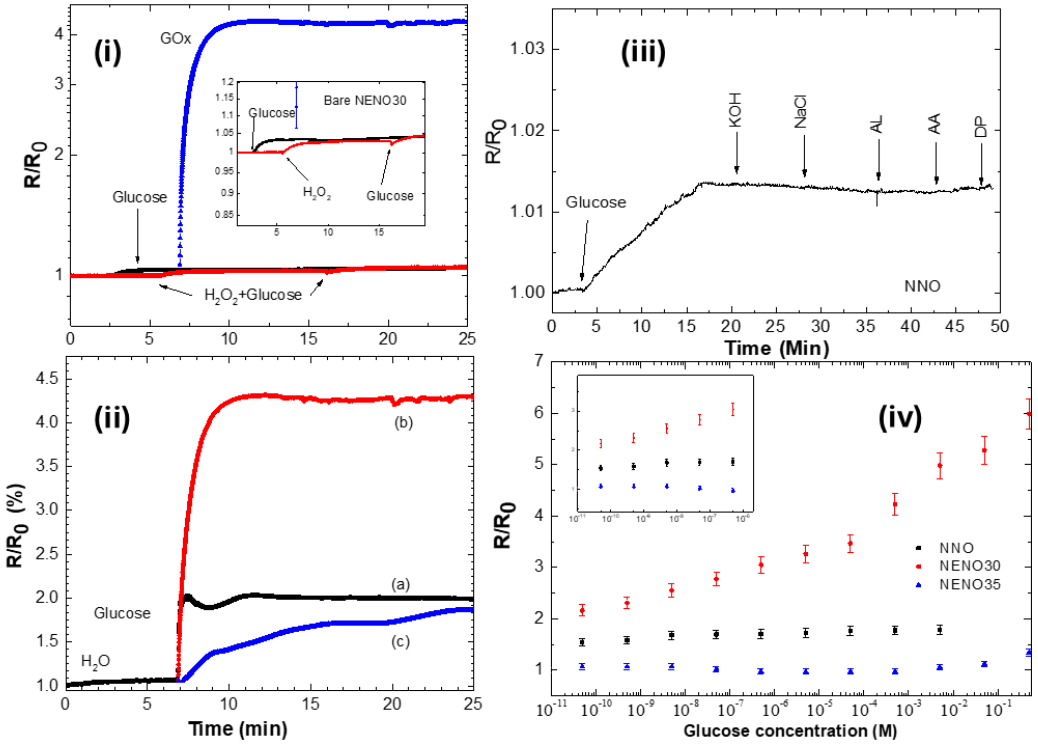


Figure 6. (**i**) R/R_0 versus time curves of pristine and GOx-modified NENO30 film with 20 µL of 0.5 M glucose solution and 0.5 M hydrogen peroxide. The inset shows the rise in the R/R_0 with the addition of glucose (black curve) and H_2O_2 (red curve), and subsequently glucose. (**ii**) Time resistance of (**a**) NNO (black), (**b**) NENO30 (red), and (**c**) NENO35 (blue) devices, decorated with GOx enzymes, with 20 µL of 0.5 M glucose added to the surface. (**iii**) Response of the sensor to the addition of 0.5 M glucose and successive addition of KOH, NaCl, Lactic acid (AL), Ascorbic acid (AA), and dopamine (DP). (**iv**) Calibration curves of R/R_0 response to changing glucose concentrations. In detail, the inset shows a magnification of R/R_0 at low glucose concentrations for the NNO-Gox and NENO35-GOx devices (noise level < 5%).

It should be noted that the enzyme is directly linked to the cysteamine molecules over the gold electrodes. The oxidation of glucose occurs locally with the GOx molecules, also continuously providing H_2O_2 localized at the nickelate surface. Additionally, the good conductivity of both the nickelate film and the gold electrode provides an excellent microenvironment for GOx, thereby enhancing the rate of electron transfer [10,40,41]. Therefore, we believe that the synergistic effect of GOx localization and H_2O_2 generation near the nickelate surface is responsible for a higher electron transfer and these higher R/R_0 values.

The reaction between H_2O_2 and the nickelate–GOx is not localized, and some authors have reported that an excess of H_2O_2 can promote a loss of enzyme activity [42]. From these discussions, we believe that the nickelate–GOx devices continue to function as a first-generation glucose biosensor.

Figure 6ii displays these curves, which show a rapid increase (~10 s) in R/R_0 until reaching a maximum plateau. This behavior indicates that at this plateau, the system reaches a constant reaction rate at the fixed glucose concentration; similar behavior has been reported for an $SmNiO_3$-GOx device in the literature [9]. Additionally, a greater change in R/R_0 was observed for the NENO30/GOx sample. These findings highlight how small changes in the electronic state influence the sensor response of this film. Zang et al. [9] correlate the modification of proton-doped nickelate thin films with a high detection limit

in enzyme–$SmNiO_3$ devices, attributing this to the strong electron correlation exhibited by the nickelate compounds.

To confirm the significance of the nickelate film in the reaction with glucose, similar measurements were conducted on different substrates, specifically SiO_2/Si(100) and ITO/PET. In this process, identical gold tracks on these substrates were functionalized with cysteamine and glucose oxidase (GOx). No change in the R/R_0 values was observed upon adding the glucose solution, as shown in Figure S3 (Supplementary Materials). These results suggest that the presence of the nickelate film is necessary for the film–GOx device to promote the glucose reaction.

To verify their specificity, nickelate–GOx devices were tested separately using 20 µL of 0.5 M galactose, fructose, and glucose. R/R_0 values change only with glucose while remaining constant with the addition of the other sugars (see Figure S4). To test the selectivity of the GOx devices, glucose detection was measured in the presence of the most common interfering species, ascorbic acid (AA) and Dopamine (DP). Typically, physiological concentrations exhibit 3–8 mM of glucose and 0.1 mM of AA [43]. Figure 6iii shows the measurement of R/R_0 vs. time using ~20 µL of 0.5M glucose, adding successively 0.1 mM of KOH, NaCl, Lactic acid (AL), AA, and DP for the NNO-GOx devices. Similar behavior was observed for Eu-doped films. These measurements show no significant change in the R/R_0 values in the presence of interferents, indicating the high selectivity of these proposed sensors.

Figure 6iv shows the response of all $Nd_{1-x}Eu_xNiO_3$–GOx devices to low glucose levels, with the R/R_0 values increasing steadily as the glucose concentration rises. This figure also indicates that NENO30-GOx devices are more sensitive to changing glucose levels. The R/R_0 versus concentration curves were used to estimate the sensitivity of the three samples (see Figure S5). The NENO30-GOx device exhibits the highest sensitivity, approximately 9.25×10^{-1} mM^{-1}, and the widest detection range (see Table 2). Across all films, R/R_0 values increase with higher glucose concentrations, with the NENO30-GOx device reaching higher R/R_0 values at elevated concentrations. For example, the electrical resistance of the NENO35-GOx device ranges from 71 kΩ to 76.6 kΩ when glucose concentrations are varied from 10^{-10} M to 0.5 M. In contrast, for NENO30-GOx sample, this R value varies from 9.7 to ~28 Ω (see Figure S5ii).

Table 2. The values listed were the sensitivity, glucose concentration range, detection limit (LOD), and the correlation coefficient (R^2) calculated for the $Nd_{1-x}Eu_xNiO_3$—GOx devices.

X	Sensitivity (mM^{-1})	Concentration Range	LOD	R^2
0.0	2.5×10^{-3}	10^{-10} to 0.5 M	4.13×10^{-5} µM	0.91
0.3	9.25×10^{-1}	10^{-11} to 0.5 M	3.57×10^{-5} µM	0.92
0.35	1.4×10^{-3}	10^{-10} to 0.5 M	7.71×10^{-5} µM	0.99

This change in the R/R_0 values with the glucose concentration may be related to changes in the electronic structure caused by Eu doping. However, as seen in SEM images, these samples seem to have slightly higher apparent porosity, which could also contribute to this result. When examining the R/R_0 response at different glucose concentrations, it is notable that the NENO30 film shows a better sensor response than the other samples, suggesting that the electronic structure near T_{MI} enhances the GOx/glucose reaction on the sample surface.

As can be seen in Figure 6iv, the R/R_0 versus glucose concentration curves exhibit a non-linear behavior with a log x-axis scale, which makes it difficult to calculate the LOD using the expression LOD = 3.3 σ/slope. The σ value is the blank standard deviation,

and the slope is observed in a linear signal-concentration curve. For non-linear curves, an estimated method is to consider that the R/R_0 intensity approaches 3.3.σ value at low concentrations [44]. The detection limit (LOD) was calculated using the ratio of the lowest concentration (10^{-10} M) and the corresponding R/R_0 value measured for the nickelates-GOx, which is equal to 3.3.σ/LOD (see Table 2). The σ value is the blank standard deviation, whose values were estimated from the R/R_0 values measured in water. These standard deviations are <3%, but we consider σ ~ 5% to include any ambient changes (humidity and temperature variation). The LOD values ranged from 3.57×10^{-5} to 7.7×10^{-5} µM for NENO30-GOx and NENO35-GOx, respectively. These values align with those reported in the literature for various electrochemical glucose sensors that utilize a perovskite-based material as their foundation.

The LOD of other perovskite-based glucose sensors is presented in Table 3. La-based perovskite biosensors exhibit the lowest limits of detection, as 8 nM was obtained for carbon paste electrodes modified with $LaNi_{0.6}Co_{0.4}O_3$ [29]. Perovskite also provides a lower detection limit for H_2O_2, showing the most excellent catalytic effect of the B-site ions Ni and Co. Other lanthanide A-site ions, such as praseodymium and neodymium, are replaced by alkaline earth metals, including barium and strontium [43].

Table 3. Examples of the performance of perovskite-based glucose biosensors.

Material	Range	LOD	Reference
$NdNiO_3$/GCE	0.0005–4.6 mM	0.3 µM	[17]
$SmNiO_3$/GOx/CysAmAm/Au	5×10^{-11}–5×10^3 µM	0.5 µM	[9]
$Sr_{1.7}Ca_{0.3}PdO_3$/Graphite	5 µM–1.4 mM	$8.45.10^{-3}$ µM	[43]
$LaNiO_3$/GCE	0.2–3240 µM	0.035 µM	[19]
$LaNi_{0.6}Co_{0.4}O_3$/CPE	0.05–200 µM	8.0×10^{-3} µM	[29]
NiO/ITO	0.01–83 mM	8.1 µM	[45]
CuO-NiO/GCE	0.2–1×10^3 µM	0.08 µM	[46]
$SrPdO_3$/AuNPs	0.1–6 mM	10.1 µM	[47]
$Nd_{1-x}Eu_xNiO_3$/GOx/CysAmAm/Au	5×10^{-6} µM–5×10^2µM	3.57×10^{-5}–7.7×10^{-5} µM	This Work

This work reports the LOD values for the $Nd_{1-x}Eu_xNiO_3$/GOx/CysAm/Au devices, which are comparable to those reported for other nickelates. However, it shows that doping with Eu^{3+} ions improves the sensor response. Notably, small changes in the crystalline and electronic structure result in shifts in the metal–insulator state of these samples at room temperature. Along with the presence of Ni^{3+} and Ni^{2+}, these factors make these materials significant as glucose sensors.

In the Supplementary Materials, the repeatability, reproducibility, and stability of the nickelate–GOx devices used as glucose sensors were also assessed (Figures S6–S8). These tests were conducted on three samples of each nickelate film, demonstrating good reproducibility and repeatability. The R/R_0 values are close to 0.9 with 0.5 M of glucose and a relative standard deviation of approximately 5%. It is worth noting that changes in temperature and humidity can cause variations in these values. Additionally, the R/R_0 values of these devices remain stable for 30 to 60 min, but their magnitude varies significantly over 14 days. This fluctuation can be linked to the connection and disconnection of the electrical cables used during these measurements.

To evaluate the practical usefulness of these nickelate–GOx sensors, we used calibration curves to compare their performance with freshly prepared orange juice (filtered with a 0.45 µm PTFE syringe filter). The calibration curve is shown in Figure 7i; here, a commercial orange juice (Natural One, with a total sugar content of 9 g/100 mL) was

used as a reference. We also tested a real sample of orange juice (OJ) and measured an R/R_0 versus OJ concentration curve. Figure 7i displays the R/R_0 versus time curve of the NENO30-GOx device after adding freshly squeezed orange juice. The R/R_0 values increase for approximately 10 min and reach a maximum at longer times. Using the calibration equation $Y = -0.80 + 0.09x$ ($R^2 = 0.97$), we estimate the glucose concentration in the natural orange juice to be 0.267(3) M (4.8 g/100mL), which is larger than the 2.6 g/100mL value reported in the literature [48]. Therefore, one possible application for these nickelate–GOx devices is to monitor glucose in fluids.

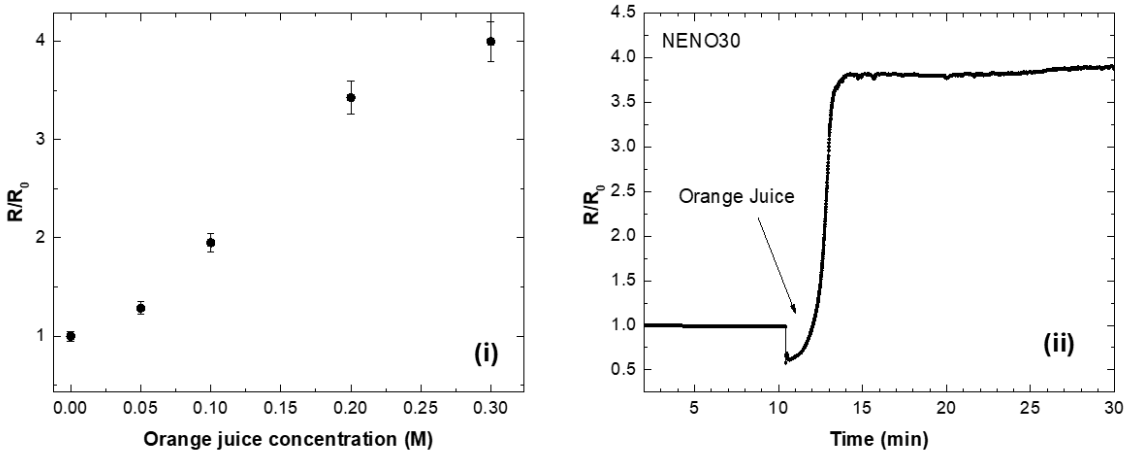


Figure 7. (**i**) Calibration curve of R/R_0 versus commercial orange juice concentration. (**ii**) Measurement of a real sample of orange juice with the NENO30-GOx device.

4. Conclusions

In summary, this study confirmed that NNO and NENO thin films can be successfully fabricated using the chemical solution deposition method. $NdNiO_3$ and $Nd_{1-x}Eu_xNiO_3$ (x = 0, 0.30, 0.35) thin films crystallize in an orthorhombic distorted perovskite structure. They exhibit physical properties, such as a metal–insulator transition, which can be tuned through Eu doping and lattice strain. Gold electrodes (~100 nm) deposited on the surface of the nickelate were functionalized with cysteamine and glucose oxidase (GOx). The electrical resistance of these nickelate–GOx films changes in response to glucose exposure, with resistance increasing as the glucose concentration rises. The sensitivity and detection limits range from 0.8 to 9×10^{-1} mM^{-1} and from 3.57×10^{-5} to 7.71×10^{-5} µM for NENO30 and NENO35, respectively. Evaluation of interference, selectivity, repeatability, and reproducibility further supports the potential of these devices for glucose sensing. For films with x = 0.30 and 0.35, the incorporation of Eu^3 into the $NdNiO_3$ matrix modifies the electronic structure, directly affecting the sensor response, which is related to the Ni^{3+}/Ni^{2+} ratio and the metal–insulator transition temperature of the nickelates. Based on these results, the nickelate–GOx devices show promise for monitoring glucose levels in fluids.

Supplementary Materials: The following supporting information can be downloaded at: https://www.mdpi.com/article/10.3390/chemosensors13110387/s1, Figures S1–S10.

Author Contributions: The work presented here was carried out as a collaboration among all authors. Conceptualization, methodology, and formal analysis, G.P.L. and M.T.E.; XPS and writing, J.H.H.R.; writing—original draft preparation, G.P.L.; writing—review and editing, M.T.E.; review and editing, I.L.N. and N.L.V.C.; funding acquisition, M.T.E. All authors have read and agreed to the published version of the manuscript.

Funding: This work was supported by a CAPES fellowship, the COVID Project UFABC, and Fundação de Amparo à Pesquisa do Estado de São Paulo (2022/11278-9).

Institutional Review Board Statement: Not applicable.

Informed Consent Statement: Not applicable.

Data Availability Statement: The data will be made available upon request.

Acknowledgments: GPL acknowledges CAPES for the fellowship, the Multiuser Center Facilities at UFABC, and Renato Altobelli Antunes for XPS measurements. We also acknowledge the financial support provided by Fundação de Amparo à Pesquisa do Estado de São Paulo (2022/11278-9) and the COVID Project UFABC (2021–2022).

Conflicts of Interest: The authors declare no conflicts of interest.

Abbreviations

The following abbreviations are used in this manuscript:

NNO	$NdNiO_3$
NENO30	$Nd_{0.7}Eu_{0.3}NiO_3$
NENO35	$Nd_{0.65}Eu_{0.35}NiO_3$
GOx	Glucose Oxidase
CysAm	Cysteamine
HRP	horseradish peroxidase

References

1. Grünblatt, E.; Ohki, C.M.Y.; Schmitt-Böhrer, G.A.; Riederer, P.; Walitza, S. Exploring the interplay of glucose metabolism, insulin resistance, and neurodegenerative pathologies: Insights from streptozotocin and hypoglycaemic in vitro models. *J. Neural Transm.* **2025**, *132*, 1479–1491. [CrossRef]
2. Collotta, D.; Ferreira Alves, G. Editorial: Unveiling the role of carbohydrates in cardiometabolic health. *Front. Nutr.* **2025**, *12*, 1568319. [CrossRef]
3. Krook, A.; Mulder, H. Pinpointing precision medicine for diabetes mellitus. *Diabetologia* **2022**, *65*, 1755–1757. [CrossRef]
4. Reddy, V.S.; Agarwal, B.; Ye, Z.; Zhang, C.; Roy, K.; Chinnappan, A.; Narayan, R.J.; Ramakrishna, S.; Ghosh, R. Recent Advancement in Biofluid-Based Glucose Sensors Using Invasive, Minimally Invasive, and Non-Invasive Technologies: A Review. *Nanomaterials* **2022**, *12*, 1082. [CrossRef]
5. Zafar, H.; Channa, A.; Jeoti, V.; Stojanović, G.M. Comprehensive Review on Wearable Sweat-Glucose Sensors for Continuous Glucose Monitoring. *Sensors* **2022**, *22*, 638. [CrossRef] [PubMed]
6. Singhal, C.M.; Kaushik, V.; Awasthi, A.; Zalke, J.B.; Palekar, S.; Rewatkar, P.; Srivastava, S.K.; Kulkarni, M.B.; Bhaiyya, M.L. Deep Learning-Enhanced Portable Chemiluminescence Biosensor: 3D-Printed, Smartphone-Integrated Platform for Glucose Detection. *Bioengineering* **2025**, *12*, 119. [CrossRef] [PubMed]
7. Ye, W.; Ruiyi, L.; Zaijun, L. Ultrasensitive electrochemical sensor for monitoring glucose in sweat based on Ta0.975Au0.025O1.05-graphene nanobelt nanocomposite with excellent catalytic activity and specificity. *Microchim. Acta* **2025**, *192*, 1–14. [CrossRef]
8. Peng, L.; Liu, Y.; Wu, Q.; Zhou, L.; Dong, M.; Zhong, L. Au-doped MoS_2 nanozyme with self-cascade catalytic performance for one-step glucose detection application. *Anal. Bioanal. Chem.* **2025**, *417*, 4945–4955. [CrossRef] [PubMed]
9. Zhang, H.-T.; Zuo, F.; Li, F.; Chan, H.; Wu, Q.; Zhang, Z.; Narayanan, B.; Ramadoss, K.; Chakraborty, I.; Saha, G.; et al. Perovskite nickelates as bio-electronic interfaces. *Nat. Commun.* **2019**, *10*, 1–7. [CrossRef]
10. Sun, Y.; Nguyen, T.N.H.; Anderson, A.; Cheng, X.; Gage, T.E.; Lim, J.; Zhang, Z.; Zhou, H.; Rodolakis, F.; Zhang, Z.; et al. In Vivo Glutamate Sensing inside the Mouse Brain with Perovskite Nickelate-Nafion Heterostructures. *ACS Appl. Mater. Interfaces* **2020**, *12*, 24564–24574. [CrossRef]
11. Xu, S.; Lee, T.R. Fe_3O_4 nanoparticles: Structures, synthesis, magnetic properties, surface functionalization, and emerging applications. *Appl. Sci.* **2021**, *11*, 11301. [CrossRef]
12. Thatikayala, D.; Ponnamma, D.; Sadasivuni, K.K.; Cabibihan, J.J.; Al-Ali, A.K.; Malik, R.A.; Min, B. Progress of Advanced Nanomaterials in the Non-Enzymatic Electrochemical Sensing of Glucose and H_2O_2. *Biosensors* **2020**, *10*, 151. [CrossRef]
13. Jahani, P.M.; Javar, H.A.; Mahmoudi-Moghaddam, H. A new electrochemical sensor based on Europium-doped NiO nanocomposite for detection of venlafaxine. *Measurement* **2021**, *173*, 108616. [CrossRef]
14. Huang, J.; Wang, S.; Ding, J.; Li, S.; Xu, J. Enhanced glucose sensing performance via synergistic integration of silver nanowires and cobalt oxide. *Surf. Interfaces* **2025**, *72*, 107065. [CrossRef]

15. Chen, T.-W.; Ramachandran, R.; Chen, S.-M.; Anushya, G.; Ramachandran, K. Graphene and Perovskite-Based Nanocomposite for Both Electrochemical and Gas Sensor Applications: An Overview. *Sensors* **2020**, *20*, 6755. [CrossRef] [PubMed]
16. Singh, Y.; Verma, S.K.; Kandadai, N.; Subbaraman, H. Highly Sensitive Graphene-Assisted Large-Area Kapton-Based Flexible Surface Plasmon Resonance Biosensor for Enzymatic Glucose Detection. *ACS Appl. Mater. Interfaces* **2025**, *17*, 45527–45537. [CrossRef]
17. Sivakumar, M.; Pandi, K.; Chen, S.-M.; Cheng, Y.-H.; Sakthivel, M. Facile synthesis of perovskite-type $NdNiO_3$ nanoparticles for an effective electrochemical non-enzymatic glucose biosensor. *New J. Chem.* **2017**, *41*, 11201–11207. [CrossRef]
18. He, J.; Sunarso, J.; Zhu, Y.; Zhong, Y.; Miao, J.; Zhou, W.; Shao, Z. High-performance non-enzymatic perovskite sensor for hydrogen peroxide and glucose electrochemical detection. *Sens. Actuat. B-Chem.* **2017**, *244*, 482–491. [CrossRef]
19. Wang, B.; Gu, S.; Ding, Y.; Chu, Y.; Zhang, Z.; Ba, X.; Zhang, Q.; Li, X. A novel route to prepare $LaNiO_3$ perovskite-type oxide nanofibers by electrospinning for glucose and hydrogen peroxide sensing. *Analyst* **2013**, *138*, 362–367. [CrossRef]
20. Boubezari, I.; Zazoua, A.; Errachid, A.; Jaffrezic-Renault, N. Sensitive Electrochemical Detection of Bioactive Molecules (Hydrogen Peroxide, Glucose, Dopamine) with Perovskites-Based Sensors. *Chemosensors* **2021**, *9*, 289. [CrossRef]
21. Catalano, S.; Gibert, M.; Fowlie, J.; Íñiguez, J.; Triscone, J.M.; Kreisel, J. Rare-earth nickelates $RNiO_3$: Thin films and heterostructures. *Rep. Prog. Phys.* **2018**, *81*, 046501. [CrossRef]
22. Vinothkumar, V.; Sakthivel, R.; Chen, S.-M. Rare earth dysprosium nickelate nanospheres for the selective electrochemical detection of antipsychotic drug perphenazine in biological samples. *Mater. Today Chem.* **2022**, *24*, 100883. [CrossRef]
23. Zhang, Z.; Schwanz, D.; Narayanan, B.; Kotiuga, M.; Dura, J.A.; Cherukara, M.; Zhou, H.; Freeland, J.W.; Li, J.; Sutarto, R.; et al. Perovskite nickelates as electric-field sensors in salt water. *Nature* **2017**, *553*, 68–72. [CrossRef] [PubMed]
24. Ha, S.D.; Shi, J.; Meroz, Y.; Mahadevan, L.; Ramanathan, S. Neuromimetic Circuits with Synaptic Devices based on Strongly Correlated Electron Systems. *Phys. Rev. Appl.* **2014**, *2*, 064003. [CrossRef]
25. de La Cruz, F.P.; Piamonteze, C.; Massa, N.E.; Salva, H.; Alonso, J.A.; Martínez-Lope, M.J.; Casais, M.T. Possible common ground for the metal-insulator phase transition in the rare-earth nickelates $RNiO_3$. *Phys. Rev. B* **2002**, *66*, 153104. [CrossRef]
26. Medarde, M.; Dallera, C.; Grioni, M.; Delley, B.; Vernay, F.; Mesot, J.; Martínez-Lope, M.J. Charge disproportionation in $RNiO_3$ perovskites (R=rare earth) from high-resolution x-ray absorption spectroscopy. *Phys. Rev. B* **2009**, *80*, 245105. [CrossRef]
27. Pandiyan, R.; Vinothkumar, V.; Chen, S.-M.; Prasad, G.V.; Kim, T.H. Perovskite lanthanum nickelate nanoparticles: As effective modified screen printed carbon electrode for electrochemical detection of trifluoperazine. *Surf. Interfaces* **2023**, *38*, 102805. [CrossRef]
28. Rossato, J.H.H.; Oliveira, M.E.; Lopes, B.V.; Gallo, B.B.; La Rosa, A.B.; Piva, E.; Barba, D.; Rosei, F.; Carreño, N.L.V.; Escote, M.T. A Flexible Electrochemical Biosensor Based on $NdNiO_3$ Nanotubes for Ascorbic Acid Detection. *ACS Appl. Nano Mater.* **2022**, *5*, 3394–3405. [CrossRef]
29. Zhang, Z.; Gu, S.; Ding, Y.; Jin, J. Analytica Chimica Acta A novel nonenzymatic sensor based on $LaNi_{0.6}Co_{0.4}O_3$ modified electrode for hydrogen peroxide and glucose. *Anal. Chim. Acta* **2012**, *745*, 112–117. [CrossRef] [PubMed]
30. García-Muñoz, J.L.; Rodríguez-Carvajal, J.; Lacorre, P.; Torrance, J.B. Neutron-diffraction study of $RNiO_3$ (R=La, Pr, Nd, Sm): Electronically induced structural changes across the metal-insulator transition. *Phys. Rev. B* **1992**, *46*, 4414. [CrossRef]
31. Chang, L.; Wang, L.; You, L.; Zhou, Y.; Fang, L.; Wang, S.; Wang, J. Band gap tuning of nickelates for photovoltaic applications. *J. Phys. D. Appl. Phys.* **2016**, *49*, 44LT02. [CrossRef]
32. Chang, L.; Wang, L.; You, L.; Yang, Z.; Abdelsamie, A.; Zhang, Q.; Zhou, Y.; Gu, L.; Chambers, S.A.; Wang, J. Tuning Photovoltaic Performance of Perovskite Nickelates Heterostructures by Changing the A-Site Rare-Earth Element. *ACS Appl. Mater. Interfaces* **2019**, *11*, 16191–16197. [CrossRef]
33. Escote, M.T.; Barbeta, V.B.; Jardim, R.F.; Campo, J. Metal-insulator transition in $Nd_{1-x}Eu_xNiO_3$ compounds. *J. Phys. Condens. Matter.* **2006**, *18*, 6117–6132. [CrossRef]
34. Yamanaka, T.; Hattori, A.N.; Pamasi, L.N.; Takemoto, S.; Hattori, K.; Daimon, H.; Sato, K.; Tanaka, H. Effects of Off-Stoichiometry in the Epitaxial $NdNiO_3$ Film on the Suppression of Its Metal-Insulator-Transition Properties. *ACS Appl. Electron. Mater.* **2019**, *1*, 2678–2683. [CrossRef]
35. Preziosi, D.; Sander, A.; Barthélémy, A.; Bibes, M. Reproducibility and off-stoichiometry issues in nickelate thin films grown by pulsed laser deposition. *AIP Adv.* **2017**, *7*, 1–17. [CrossRef]
36. Qiao, L.; Bi, X. Direct observation of oxygen vacancy and its effect on the microstructure, electronic and transport properties of sputtered $LaNiO_3$-δ films on Si substrates. *Thin Solid Films* **2010**, *519*, 943–946. [CrossRef]
37. Medarde, M.L. Structural, magnetic and electronic properties of perovskites (R = rare earth). *J. Phys. Condens. Matter.* **1997**, *9*, 1679–1707. [CrossRef]
38. Capon, F.; Ruello, P.; Bardeau, J.F.; Simon, P.; Laffez, P.; Dkhil, B.; Ratuszna, A. Metal–insulator transition in thin films of $R_xR_{1-x}'NiO_3$ compounds: DC electrical conductivity and IR spectroscopy measurements. *J. Phys. Condens. Matter.* **2005**, *17*, 1137–1150. [CrossRef]

39. Barbeta, V.B.; Jardim, R.F.; Escote, M.T.; Dilley, N.R. Magnetothermopower in $Nd_{1-x}Eu_xNiO_3$ compounds. *J. Appl. Phys.* **2007**, *101*, 09N509. [CrossRef]
40. Salimi, A.; Sharifi, E.; Noorbakhsh, A.; Soltanian, S. Immobilization of glucose oxidase on electrodeposited nickel oxide nanoparticles: Direct electron transfer and electrocatalytic activity. *Biosens. Bioelectron.* **2007**, *22*, 3146–3153. [CrossRef]
41. NNjoko, N.; Louzada, M.; Britton, J.; Khene, S.; Nyokong, T.; Mashazi, P. Bioelectrocatalysis and surface analysis of gold coated with nickel oxide/hydroxide and glucose oxidase towards detection of glucose. *Colloids Surfaces B Biointerfaces* **2020**, *190*, 110981. [CrossRef]
42. Guoqiang, G.; Liang, Q.; Yani, Z.; Pengyun, W.; Fanzhuo, K.; Yuyang, Z.; Zhiyuan, L.; Xing, N.; Xue, Z.; Qiongya, L.; et al. Recent advances in glucose monitoring utilizing oxidase electrochemical biosensors integrating carbon-based nanomaterials and smart enzyme design. *Front. Chem.* **2025**, *13*, 1591302. [CrossRef]
43. El-Ads, E.H.; Galal, A.; Atta, N.F. The effect of A-site doping in a strontium palladium perovskite and its applications for non-enzymatic glucose sensing. *RSC Adv.* **2016**, *6*, 16183–16196. [CrossRef]
44. Kong, D.; Zhao, J.; Tang, S.; Shen, W.; Lee, H.K. Logarithmic Data Processing Can Be Used Justifiably in the Plotting of a Calibration Curve. *Anal. Chem.* **2021**, *93*, 12156–12161. [CrossRef]
45. Franceschini, F.; Taurino, I. Nickel-based catalysts for non-enzymatic electrochemical sensing of glucose: A review. *Phys. Med.* **2022**, *14*, 100054. [CrossRef]
46. Nemati, S.S.; Dehghan, G.; Rashtbari, S.; Tan, T.N.; Khataee, A. Enzyme-based and enzyme-free metal-based glucose biosensors: Classification and recent advances. *Microchem. J.* **2023**, *193*, 109038. [CrossRef]
47. El-Ads, E.H.; Galal, A.; Atta, N.F. Electrochemistry of Glucose at Gold Nanoparticles Modified Graphite/$SrPdO_3$ Electrode—Towards a Novel Non-Enzymatic Glucose Sensor. *J. Electroanal. Chem.* **2015**, *749*, 42–52. [CrossRef]
48. Amor-Gutiérrez, O.; Costa-Rama, E.; Fernández-Abedul, M.T. Full integrated sampler and dilutor in an electrochemical paper-based device for glucose sensing. *Microchim. Acta* **2021**, *188*, 1–8. [CrossRef]

Disclaimer/Publisher's Note: The statements, opinions and data contained in all publications are solely those of the individual author(s) and contributor(s) and not of MDPI and/or the editor(s). MDPI and/or the editor(s) disclaim responsibility for any injury to people or property resulting from any ideas, methods, instructions or products referred to in the content.